Visualization of CO_2 and oil immiscible and miscible flow processes in porous media using NMR micro-imaging

Zhao Yuechao, SongYongchen*, Liu Yu, Jiang Lanlan and Zhu Ningjun

Key Laboratory of Ocean Energy Utilization and Energy Conservation of the Ministry of Education, Dalian University of Technology, Dalian, Liaoning 116024, China

Abstract: CO_2 flooding is considered not only one of the most effective enhanced oil recovery (EOR) methods, but also an important alternative for geological CO_2 storage. In this paper, the visualization of CO_2 flooding was studied using a 400 MHz NMR micro-imaging system. For gaseous CO_2 immiscible displacement, it was found that CO_2 channeling or fingering occurred due to the difference of fluid viscosity and density. Thus, the sweep efficiency was small and the final residual oil saturation was 53.1%. For supercritical CO_2 miscible displacement, the results showed that piston-like displacement occurred, viscous fingering and the gravity override caused by the low viscosity and density of the gas was effectively restrained, and the velocity of CO_2 front was uniform. The sweep efficiency was so high that the final residual oil saturation was 33.9%, which indicated CO_2 miscible displacement could enhance oil recovery more than CO_2 immiscible displacement. In addition, the average velocity of CO_2 front was evaluated through analyzing the oil saturation profile. A special core analysis method has been applied to in-situ oil saturation data to directly evaluate the local Darcy phase velocities and capillary dispersion rate.

Key words: NMR micro-imaging, porous media, CO_2 flooding, enhanced oil recovery, saturation

1 Introduction

CO_2 is a major contributor to the greenhouse effect leading to global warming. Enhanced Oil Recovery (EOR) using CO_2 has been an important alternative for geological CO_2 storage. CO_2 flooding is considered one of the most effective tertiary recovery processes in light/medium oil reservoirs and has been widely used. CO_2 is injected into a reservoir to increase production by reducing oil viscosity and providing miscible or immiscible displacement of the oil. However, the complicated displacement mechanisms have not been fully understood.

Traditionally, core analysts have been forced to assume that those objects were homogeneous black boxes. Volume and composition of fluids that were injected and recovered could be measured, but how the fluids were distributed and moving inside the core could only be inferred. With techniques such as noninvasive neutron radiography (Brunner and Mardock, 1946), X-ray (Morgan et al, 1950; Laird and Putuan, 1951), gamma ray, and microwave absorption, it became possible to obtain one-dimensional fluid saturation and solute distribution data. The development of X-ray computerized tomography (CT) allowed for determination of two-dimensional and three-dimensional rock densities, saturations of fluids, and concentrations of solutes (Wellington and Vinegar, 1985, 1987; Hunt and Bajsarowicz, 1988) in the core. Recently X-ray CT had been carried out to investigate CO_2 foam flow in a consolidated Bentheimer sandstone core saturated with surfactant solution (Carretero-Carralero et al, 2007; Du et al, 2007; 2008). However, since this method is sensitive to mass density contrast, experiments usually have to be carried out with large tracer concentrations leading to unwanted fingering (Wooding, 1969; Perkins and Johnston, 1969) and change of the fluid properties (Kantzas, 1995). It is because the X-ray attenuation is principally determined by the atomic number of the sample nuclei and is, therefore, dominated by the rock matrix rather than the CO_2 or oil.

NMR imaging is similar to X-ray CT in that two-dimensional and three-dimensional images can be obtained from selected regions of an object. However, X-ray CT can only image electron density and atomic number, while NMR imaging, besides spin density of a variety of nuclei (^{1}H, ^{19}F, ^{23}Na, ^{31}P, etc.), also measures a number of other quantities such as relaxation times and chemical shifts (Vinegar, 1986; Blackband et al, 1986). It is inherently more informative than radiographic techniques. It is also much less hazardous.

Special features of many NMR imaging techniques include the ability to measure the fluid flow velocities and to distinguish different liquids using their differences in intrinsic NMR properties. This type of information would be difficult to obtain by other methods. NMR imaging is a powerful analytical tool for noninvasive multidimensional visualization of flow and transport in porous media (Callaghan, 1994). NMR imaging can provide unprecedented quantitative information about fluid-phase distributions in porous media during displacement processes, as well as information about rock structure corresponding to local regions within porous media. Such information can significantly advance our understanding of the storage and transport of multiphase fluids in porous media (Chen et al, 1992; 1993). So in the past two decades, there have been many studies of visualization of flow and transport in porous media using NMR imaging techniques, for example, the transfer and fluid flow behavior during water flooding in fractured rock or rock of various wettability was experimentally investigated using NMR imaging technique (Fernø et al, 2007; Brautaset et al, 2008a; Aspenes et al, 2008). Some research was done on visualization of water flooding and polymer flooding through unconsolidated porous media using the unique centric scan SPRITE NMR imaging technique and to quantify in-situ fluid saturation distribution in rocks (Romero-Zeron et al, 2009; 2010). The distribution of remaining oil and NMR relaxation characteristic following a CO_2 miscible displacement of crude oil in San Andres crystalline dolomite cores were investigated using NMR imaging (Hazlett et al, 1993). Restricted by the condition of the experimental high-pressure core holder, it could not monitor dynamic fluid-phase distributions in porous media during displacement processes. Until recently, by using the high-pressure core holder, only few studies were done on the behavior of two-phase flow in porous media at high pressure using NMR imaging. Some research was done on the behavior of CO_2 and water two-phase flow in porous media (Suekane et al, 2005; 2006; 2009). The fluid

saturation distributions and the flow characteristics in-situ were investigated and monitored during waterfloods and subsequent injection of either liquid or supercritical CO_2 in four Portland Chalk core samples at different wettabilities using NMR imaging (Brautaset et al, 2008b).

Due to the complicated displacement mechanisms involved during CO_2 injection, the need for in-situ data is of great importance in order to fully understand the displacement process. In this study, tests have been conducted on gaseous CO_2 immiscible displacement and supercritical CO_2 miscible displacement in high-permeability sand packs. NMR imaging has been utilized to qualitatively monitor the displacement processes. This article addresses the application of the NMR imaging technique to qualitatively monitor fluid propagation and dynamic oil saturation profile during CO_2 flooding in sand pack core models.

2 Experimental

2.1 Experimental apparatus

A simplified schematic diagram of the experimental setup is shown in Fig. 1. The experimental setup consisted of two circuits, namely, the displacement line and the temperature control line. In the displacement line, the liquid CO_2 was forced into a transfer vessel in a thermostatic chamber by a CO_2 pump, and then oil and CO_2 was forced into the sand-pack cell by a syringe pump. The flow rate and back pressure were controlled by pumps and a back pressure regulator. The pressure drop through the sand pack was measured with a low differential pressure transmitter.

In the temperature control line, fluorinert FC-40 was used to control the temperature of the sand-pack cell because fluorinert contains no hydrogen atoms, thus it is not imaged, and its low dielectric properties minimize radio frequency (RF) losses (Suekane et al, 2005; Baldwin et al, 2009; Ersland et al, 2010). This fluid was maintained at a constant flow rate while being circulated through the thermostatic bath system
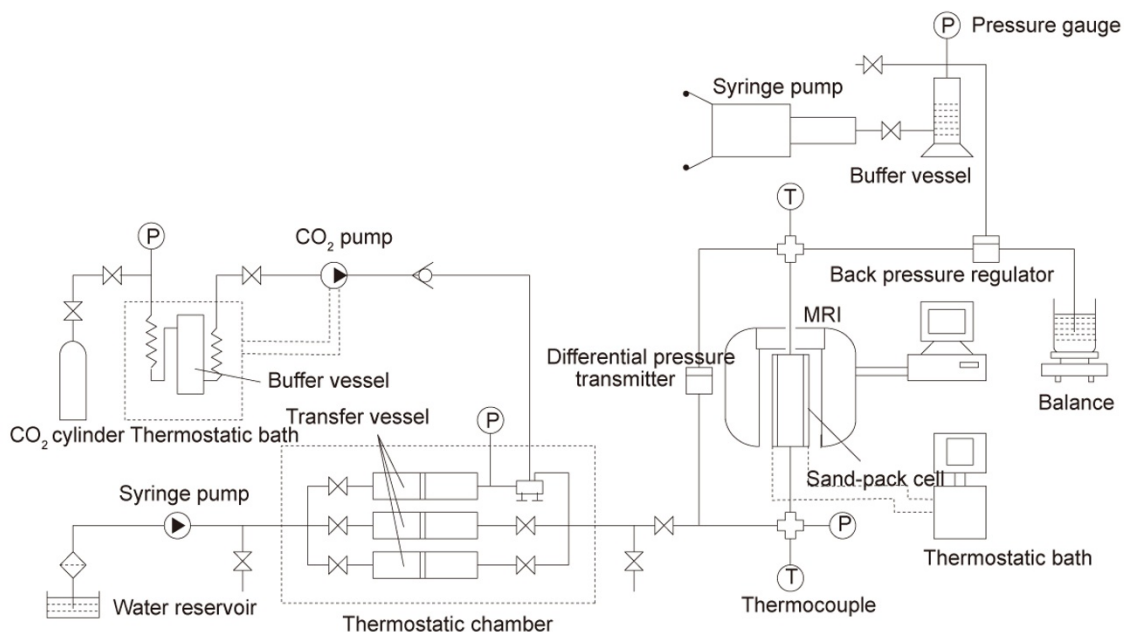
Fig. 1 A simplified schematic of the experimental setup

and around the sand-pack cell by a recirculation pump.

In this study, a new high-pressure sand-pack cell was designed and constructed for the Varian NMR Systems with a RF probe of 40 mm inner diameter. The new high-pressure sand-pack cell and its cross-sectional diagram are shown in Fig. 2. The cell was designed and constructed for NMR imaging measurements. It was inserted vertically into the NMR imaging system as shown in Fig. 1. The maximum working pressure and temperature of the sand-pack cell were 15 MPa and 70 °C, respectively. The cell consisted of water fittings (1), end cap (2), sealing O-rings (3, 4, 6, 10, and 11), end pieces (5), filter screen (7), high-pressure polyimide tube (8), and normal-pressure polyimide sleeve (9). The high-pressure polyimide tube was 200 mm long and 15 mm in inner diameter. The tube material was nonmagnetic and hence should not interfere with the RF signals used in the experiments. Temperatures at the inlet and exit of the sand-pack cell were measured with thermocouples.
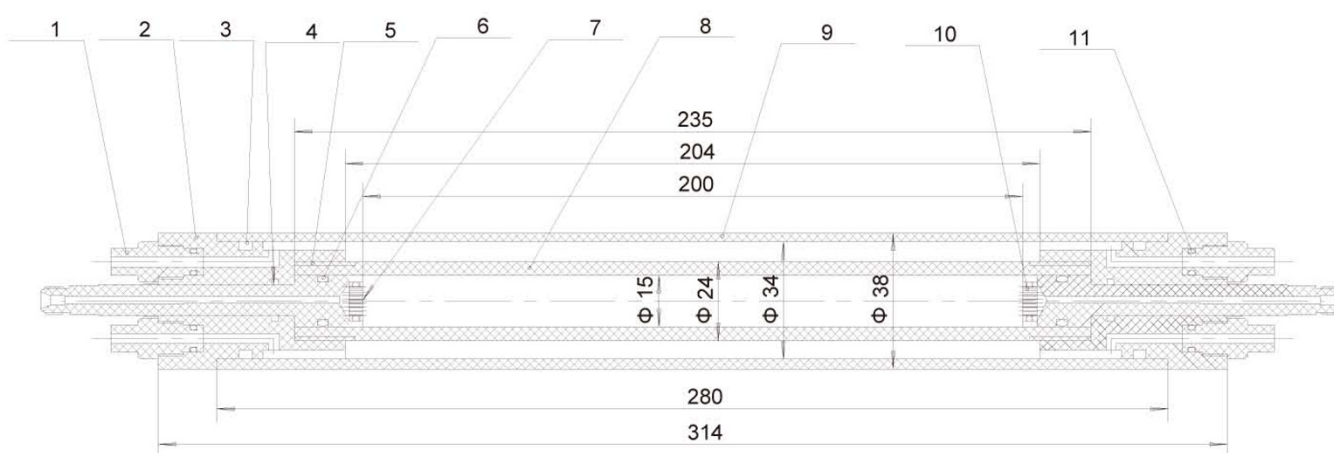
Fig. 2 The high-pressure NMR imaging sand-pack cell (unit: mm)
1-Water fittings; 2-End cap; 3, 4, 6, 10, 11-Sealing O-rings; 5-End pieces;
7-Filter screen; 8-High-pressure polyimide tube; 9-Normal-pressure polyimide sleeve

2.2 Experimental materials

Unconsolidated, high-permeability sand packs were used to evaluate oil displacement in porous media. The sand packs were prepared by packing 0.177-0.250 mm Soda-glass beads (BZ02, made in Japan) into the cylindrical cell. CO_2 (99% purity) was used as the gas phase, and n-Decane was used as the oil phase. Fluid properties, including densities and viscosities at relevant temperatures and pressures, are listed in Table 1. The glass bead-packed models had a porosity of 35.2%, which was calculated from a traditional gravimetric method, and an absolute permeability to water of 13.5 D.

Table 1 Fluid properties

Fluid	Pressure MPa	Temperature °C	Density g/cm³	Viscosity cP
CO_2	5.4	40	0.127	0.017
	8.1	40	0.29	0.023
n-Decane	5.4	40	0.72	0.74
	8.1	40	0.72	0.76

The critical point of CO_2 is at 31.1 °C and 7,398 kPa. The minimum miscible pressure (MMP) for the n-Decane/CO_2 system has been determined at 35 °C and 7,329 kPa (Asghari and Torabi, 2008) and at 37.8 °C and 7894 kPa (Ayirala et al, 2006). In the tests, the temperature of 40 °C and pressure of 5.4 MPa were selected to ensure gas properties of CO_2 for the CO_2 (gas) immiscible displacement test. The temperature of 40 °C and pressure of 8.1 MPa were selected to ensure the supercritical properties for the supercritical CO_2 miscible displacement test.

2.3 NMR imaging technique

All NMR imaging measurements were performed on a Varian NMR system with 9.4 Tesla, wide-bore (89 mm in diameter), vertical superconducting magnet. A ^1H 40 mm Millipede vertical micro-imaging probe was used and the gradient coils provided a maximum gradient strength of 50 G/cm. The NMR imaging was conducted by the fast spin echo multi-slice pulse sequence (FSEMS) during flooding and the experimental conditions are as follows: echo time (TE) 2.66 ms, repetition time (TR) 1 s, image data matrix 192×192, field of view (FOV) 40mm×40mm with 1 mm

thickness, number of slices 15 (the position of slices is shown in Fig. 3), spatial resolution $0.21 \times 0.21 \times 1$ mm^3, number of images for averaging 1, acquisition time 24 s. The bulk relaxation times were measured with the CPMG method (Carr and Purcell, 1954; Meiboom and Gill, 1958). When the sand pack was 100% saturated with oil, the spin-spin relaxation time (T_2) was 55 ms. When the sand pack was 33% saturated with oil, T_2 was 22 ms. T_2 changed with oil saturation, but TE used in this study was about eight times smaller than the bulk T_2. The sand pack did not have large T_2 distribution due to fairly uniform diameter of the glass beads used, the inhomogeneity of the magnetic field caused by the susceptibility gradients would be largely refocused by the 180 pulse. So we treated the images as spin density images and the quantitative analysis of saturation was true.

Oil contained in the sand pack was visualized in planes along the flow direction. However, these traditional NMR imaging methods fail in actual rocks with paramagnetic impurities, since the transverse signal lifetimes of these rocks are too short to be detected. Quantitative information is the ultimate goal for rock core analysis. The single-point ramped imaging with T_1 enhancement (SPRITE) imaging technique has proven to be a very robust and flexible method for the study of a wide range of systems with short signal lifetimes. As a pure phase-encoding technique, SPRITE is largely immune to image distortions generated by susceptibility variations, chemical shift, and paramagnetic impurities, unlike clinical magnetic resonance imaging methods. It enables systems with transverse lifetimes as short as tens of microseconds to be successfully visualized (Chen et al, 2006).
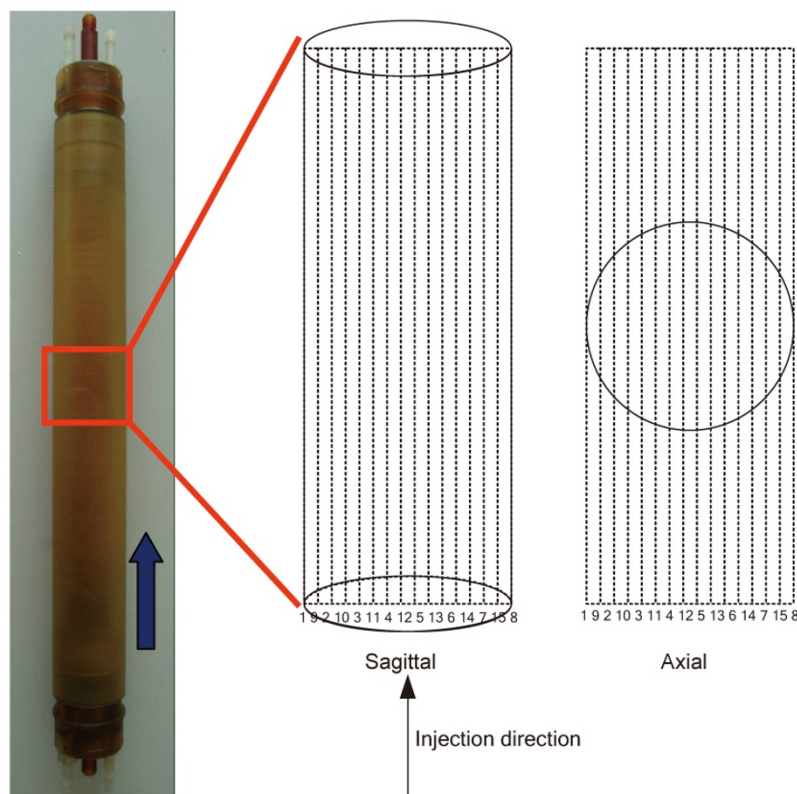
Fig. 3 Sketch map for the position of slices

3 Results and discussion

3.1 Immiscible displacement by gaseous CO$_2$

3.1.1 NMR image analysis

In the immiscible displacement process, gaseous CO_2 was injected vertically upward into the sand pack saturated with oil at 5.4 MPa and 40 °C. The injection rate of CO_2 was maintained at 0.1 mL/min. Fig. 4 shows a series of NMR images that illustrate oil saturation after different pore volumes (PV) of CO_2 were injected into the sand pack. The CO_2 moved rapidly upwards due to low fluid viscosity and high buoyancy, and then the CO_2 broke through the sand pack in the field of view (FOV). Because the sand pack was not perfectly homogenous, the injected CO_2 tended to channel

through the high-permeable zones. Therefore, some thin channels were formed and CO_2 ran through the channels vertically in a short period according to the images (b) and (c) in Fig. 4. Once these channels were being formed, the secondary oil desaturation started, CO_2 would continuously run through these channels as shown in the images (d) and (e) in Fig. 4, bypassing most of the residual oil in the matrix. The oil saturation decreased gradually and the residual oil tended to be immobilized.

3.1.2 Saturation profiles

To quantitatively analyze the evolution of oil saturation along the sand pack, the NMR imaging data was converted into saturation profiles in the manner described by Suekane et al (2009). The NMR signal intensity from any local position was proportional to the oil content in the porous media. This

(a) 0 PV   (b) 0.08 PV   (c) 0.21 PV

(d) 0.48 PV   (e) 0.90 PV   (f) 1.59 PV

0   1

NMR signal intensity/arbitrary unit
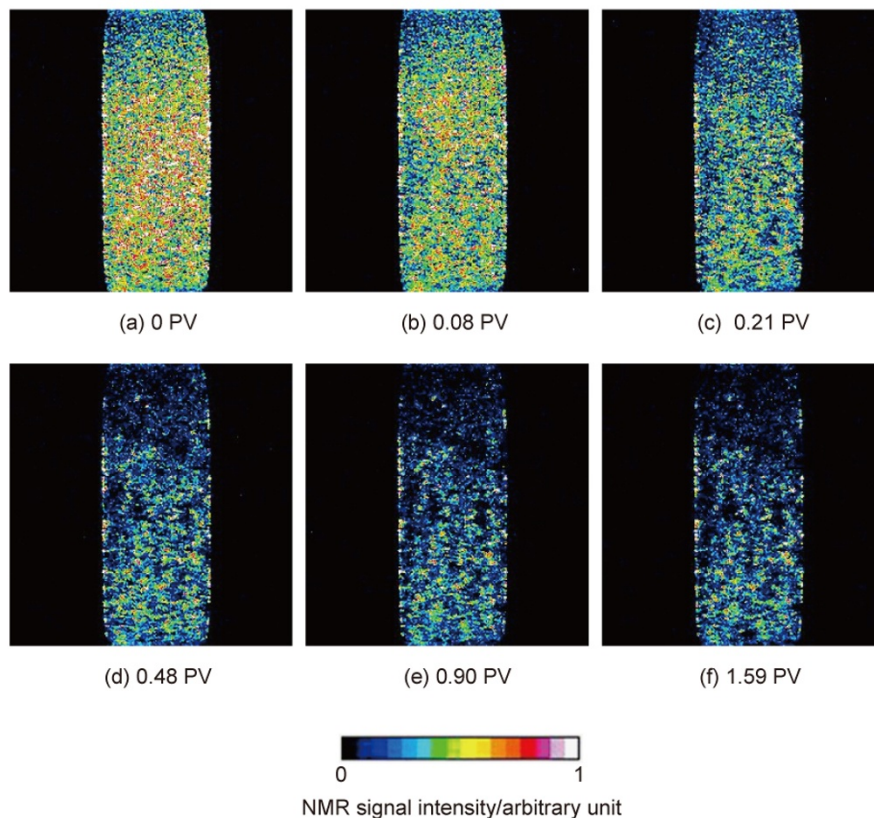
Fig. 4 Distribution of NMR signal intensity in the sand pack at 5.4 MPa, 40 °C with gaseous CO_2 injection rate of 0.1 mL/min

means that the measured NMR signal intensity reflects the local oil saturation in the porous media. In the experiments, the distribution of the initial NMR signal intensity in the porous media saturated with oil was obtained. Then, CO_2 was injected into the porous media with time-series acquisition of NMR images. The injected CO_2 would displace some oil in the porous media, thus leading to a decrease in the NMR signal intensity. First, the NMR signals of all the 15 slices were added together, corresponding to the obtained two-dimensional projective distribution of three-dimensional oil saturation distribution in the sand pack, then the oil saturation

in each pixel was calculated as the ratio of the NMR signal with the CO_2 to that without the CO_2 ($t = 0$). Next, the oil saturation was added in a lateral direction within the sand pack, that is, for a given position z along the flow direction from the inlet of the sand pack ($z = 0$). One-dimensional saturation profiles along the sand pack at different injection volume of CO_2 was obtained and shown in Fig. 5(a). Finally, the oil saturation was also averaged in the total FOV. The saturation profile of total FOV versus injection volume of CO_2 was obtained and shown in Fig. 5(b).

The oil saturation profiles in the sand pack at 5.4 MPa,

(a)   (b)
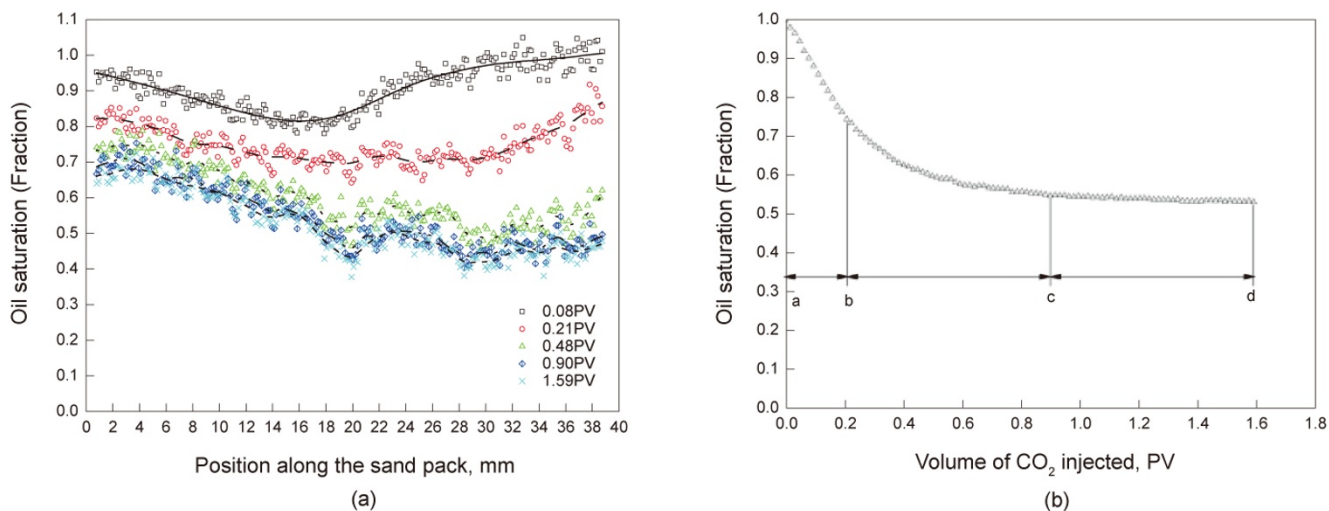
Fig. 5 Evolution of oil saturation profiles in the sand pack at 5.4 MPa, 40 °C with gaseous CO_2 injection (a) one-dimensional saturation profile along the sand pack, profiles were obtained by piecewise spline fitting; (b) saturation profile of total FOV versus volume of CO_2 injected

40 ºC with CO_2 injection were obtained and shown in Fig. 5. Fig. 5(a) shows two stages of the oil displacement by CO_2. In the first stage, starting from the beginning of the injection up to the CO_2 breakthrough, the CO_2 tended to penetrate through the more permeable regions. The second stage started after CO_2 breakthrough and ended with the unchanged oil saturation distribution. Finally, the residual oil saturation in the inlet of the sand pack before the 20 mm was higher compared to the outlet in the migration direction.

Fig. 5(b) shows oil saturation in the total FOV as a function of volume of CO_2 injection determined from NMR imaging. The profile of the CO_2 motion can also be divided into three regions. In part ab, starting from the beginning of the injection up to the CO_2 breakthrough, the oil saturation decreased linearly from 100% to 74.4% after the CO_2 injection of 0.21 PV (0.52 mL). In part bc, the oil saturation decreased exponentially to 54.8% with the CO_2 injection of 0.69 PV (1.72 mL). In part cd, continuous displacement of oil during CO_2 flooding until residual oil saturation (53.1%) was reached (oil flow ceases), the additional injection of 0.69 PV (1.72 mL) of gas recovered only little oil because at this point the relative permeability to oil was near to zero since oil saturation was equal to residual oil saturation, and oil would not flow. The final oil recovery was 46.9%.

3.2 Supercritical CO_2 miscible displacement test

3.2.1 NMR image analysis

In the CO_2 miscible displacement test, supercritical CO_2 was injected vertically upward into the oil-saturated sand pack at a rate of 0.1 mL/min (at 8.1 MPa and 40 °C). To obtain detailed information about the dynamic CO_2 displacement in the sand pack, the NMR images of oil distribution in the slices in the longitudinal direction were examined. Fig. 6 shows a series of NMR images, which illustrate the oil saturation at different injection volumes of CO_2 of 0, 0.26, 0.32, 0.48, 0.61, 0.76, 1.25, and 3.20 PV (corresponding time series was 0, 408, 504, 744, 936, 1,152, 1,896, and 4,800 s, respectively). The bright regions (orange and yellow) indicate the high NMR signal intensity corresponding to high oil saturation, while the dark regions (blue) stand for the low oil saturation. For instance, the first image shows the sand pack was 100% saturated with oil. The porosity distribution shown in Fig. 7 was calibrated with a reference standard of known porosity that was imaged with the sand pack. Then, with the injection of supercritical CO_2, the piston-like displacement occurred, the phenomenon of viscous fingering and gravity override caused by the low viscosity and density of the gas was effectively restrained, thereby diverting the injected CO_2 to lower-permeability zones and improving displacement efficiency.

3.2.2 Saturation profiles

Fig. 8(a) shows two stages of the oil displacement by supercritical CO_2. In the first stage from the beginning of the injection up to the CO_2 breakthrough, piston-like displacement occurred. As can be seen from the profile of 0.61 PV in Fig. 8(a), this stage consisted of three regions: (a) a region with low oil saturation, where the front of CO_2 has passed; (b) a region with high oil saturation, where the front of CO_2 has not yet arrived; and (c) a transition region, where the front of CO_2 is located. With CO_2 injection, the oil saturation
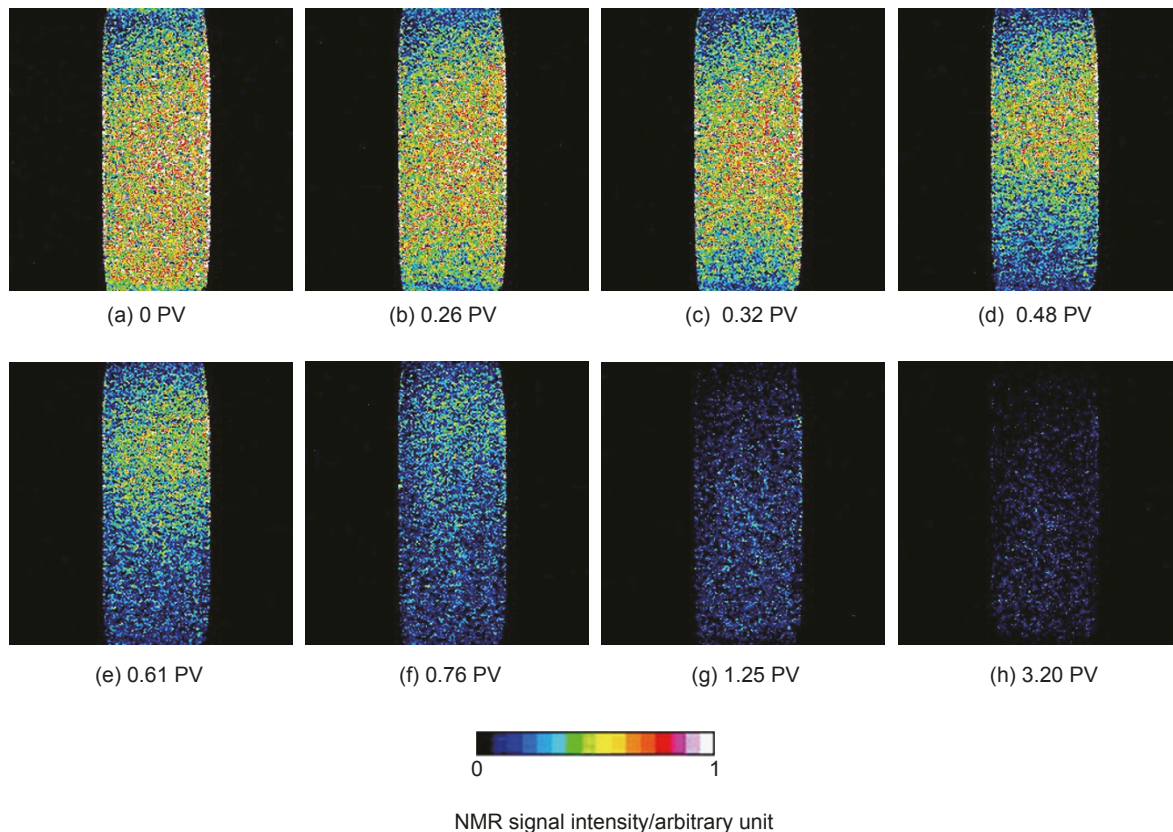
Fig. 6 Distribution of NMR signal intensity in the sand pack displaced by supercritical CO_2
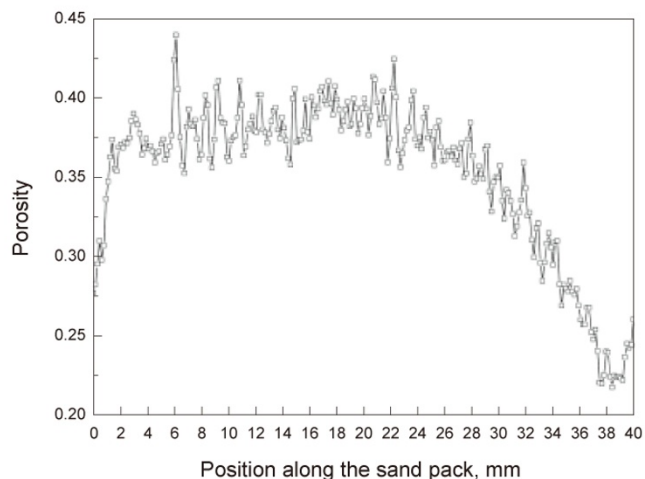
Fig. 7 One-dimensional distribution profile of porosity along the sand pack

decreased gradually from the inlet of the sand pack, and the low oil saturation region increased gradually. The front of CO_2 proceeding in the sand pack can be measured clearly. The slope of the front tended to be at a shallow angle to the migration direction. The second stage started after CO_2 breakthrough, and ended with the unchanged oil saturation distribution. This stage was characterized by secondary

oil desaturation which started in the inlet of the sand pack and propagated toward the outlet. Finally, the oil saturation decreased down to about 30%-40%.

Fig. 8(b) shows oil saturation in the total FOV as a function of the volume of supercritical CO_2 injection (or time) determined from NMR imaging. This figure shows the oil saturation decreased gradually with the injection of CO_2, and continuous displacement of oil during CO_2 displacement until residual oil saturation (33.9%) was reached (oil flow ceases) after the injection of 3.2 PV of CO_2. In the oil saturation profile, four characteristic stages can be found when CO_2 front moved through the FOV (the total height of the sand pack is 200 mm and the height of the FOV is only 40 mm, the FOV is located at the centre of the sand pack), which were showed in Fig. 6 (real schematic) and Fig. 9 (simplified schematic). These stages are when (a) the head of CO_2 displacement front moved into the FOV; (b) the tail of CO_2 displacement front moved into the FOV; (c) the head of CO_2 displacement front broke through the FOV; (d) the tail of CO_2 displacement front broke through the FOV. So the process of the supercritical CO_2 motion can be divided into four regions as follows: in part ab, the oil saturation decreased gradually from 100% to 95% with the injection of CO_2, the decrease in the oil saturation was more rapid in the end of the part AB due to irregular characteristics of the CO_2 front; in part
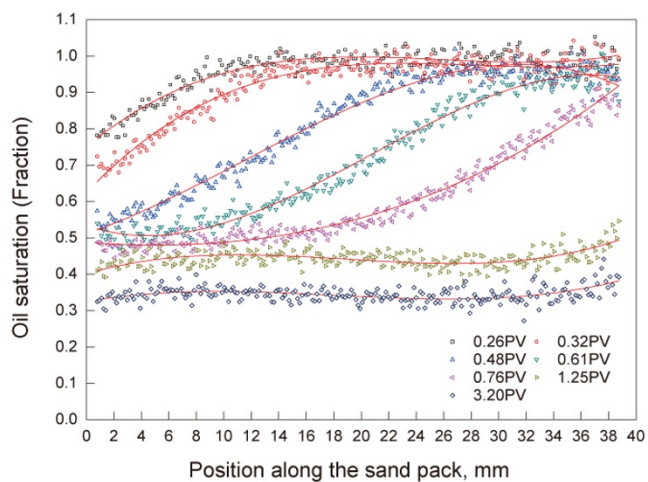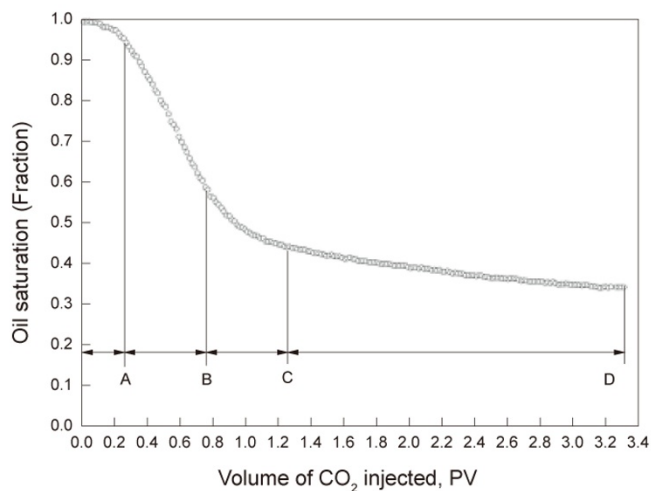
Fig. 8 Evolution of oil saturation profiles in the sand pack at 8.1 MPa, 40 °C with supercritical CO_2 injection (a) one dimensional saturation profile along the sand pack, profiles were obtained by polynomial fitting; (b) saturation profile of total FOV versus volume of CO_2 injected
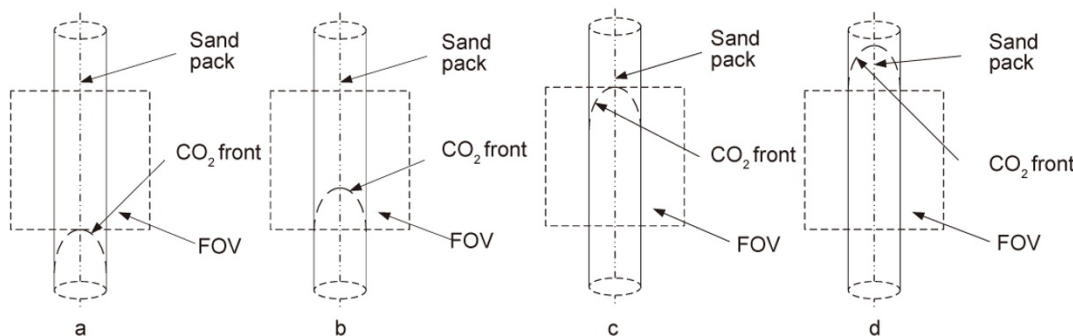
Fig. 9 Simplified schematics of the characteristic times during CO_2 front moved through the FOV

BC, the oil saturation decreased linearly to 58.5% due to the uniform velocity of CO_2 front; in part CD, the oil saturation decreased exponentially to 43.8% with the process of total CO_2 displacement front breakthrough; in part DE, the oil saturation steady decreased to 33.9% with the process of secondary oil desaturation. The final oil recovery was 66.1%. The sweep efficiency in this test with supercritical CO_2 miscible displacement was higher than that of the gaseous CO_2 immiscible displacement test.

Through analyzing part BC in the oil saturation profile, we can evaluate the approximate whole average velocity of CO_2 front in the following manner. The variation of oil volume (ΔV_o) in the FOV can be expressed as follows:

$$\Delta V_o = A\phi\Delta h \tag{1}$$

where A is the cross-sectional area of the sand pack, cm^2; ϕ is the porosity, fraction; Δh is the displacement of CO_2 front, cm.

The variation of CO_2 volume (ΔQ) in the FOV can be expressed as follows:

$$\Delta Q = \frac{q\Delta t}{V_p} \tag{2}$$

where q is the injection rate of CO_2, cm^3/s; Δt is the time variation, s; V_p is the pore volume of the sand pack, cm^3.

The oil saturation (S_o) can be expressed as follows:

$$S_o = \frac{V_o}{V_p} \tag{3}$$

where V_o is the oil volume in the sand pack, cm^3.

From Eqs. (1)-(3), we can evaluate the approximate whole average velocity of CO_2 front ($\bar{v}$):

$$\bar{v} = \frac{\Delta h}{\Delta t} = -\frac{\Delta S_o}{\Delta Q}\frac{q}{A\phi} \tag{4}$$

where ΔS_o is the variation of oil saturation in the FOV, fraction.

$\frac{\Delta S_o}{\Delta Q}$ in Eq. (4) can be obtained by assuming oil saturation is linear with the volume of CO_2 injection. Then we can obtain the approximate whole average velocity of CO_2 front, which is 0.12 cm/min.

Table 2 summarizes oil recovery results with the four parts of supercritical CO_2 injection for the total experimental process. In part BC, the oil recovery values obtained from the NMR imaging technique and material balance are 36.5% and 35.4%, respectively. The deviation is only 3%.

Table 2 Oil recovery with supercritical CO_2 injection

Characteristic regions	Volume of CO_2 injected, mL	Volum of CO_2 injected, PV	Oil recovery based on NMR imaging, %	Oil recovery based on material balance, %
AB	0.65	0.26	5	—
BC	1.24	0.5	36.5	35.4
CD	1.22	0.49	14.7	—
DE	4.85	1.95	9.9	—
Total	7.96	3.2	66.1	—

3.2.3 Core analysis methods

The coreflood interpretation method proposed by Goodfield et al (2001) was applied to the data generated from core displacement tests to determine the local Darcy phase velocities in the sand pack. The phase volumes per unit cross-sectional area between the core inlet (ζ=0) and the current position (ζ=z) are given by:

$$V_g(z,t) = \int_0^z \phi(\zeta)S_g(\zeta,t)\mathrm{d}\zeta \tag{5}$$

where $\phi(z)$ is the porosity at position z shown in Fig. 7 and $S_g(\zeta,t)$ is the CO_2 saturation at position z and time t shown in Fig. 8(a). Using a material balance approach, the local Darcy phase (CO_2 and oil) velocities can then be expressed in the following form:

$$U_g(z,t) = U(t)F_g^{\text{inj}}(t) - \frac{\partial V_g(z,t)}{\partial t} \tag{6}$$

$$U_o(z,t) = -\frac{\partial V_o(z,t)}{\partial t} \tag{7}$$

where $U_g(z,t)$ and $U_o(z,t)$ are the local Darcy phase velocities of CO_2 and oil, respectively; $U(t)$ is the total Darcy velocity. and $F_g^{\text{inj}}(t)$ is the fractional flow of CO_2 injection at time t. Then, the local Darcy phase velocities of CO_2 and oil were obtained with this method and shown in Fig. 10.

Darcy's law in the new interpretation methods for the phase velocities is expressed according to:

$$U_\alpha = -k\lambda_\alpha(\frac{\partial p_\alpha}{\partial z} + \rho_\alpha g) \tag{8}$$

where α denotes each phase of CO_2 (g) and oil (o); U is the local Darcy velocity; λ_a is the mobility, $\lambda_a=k_{ra}/\mu_a$; k is the absolute permeability; p is the pressure; ρ is the density; g is the gravitational acceleration; k_r is the relative permeability; μ is the viscosity.

(a)

(b)
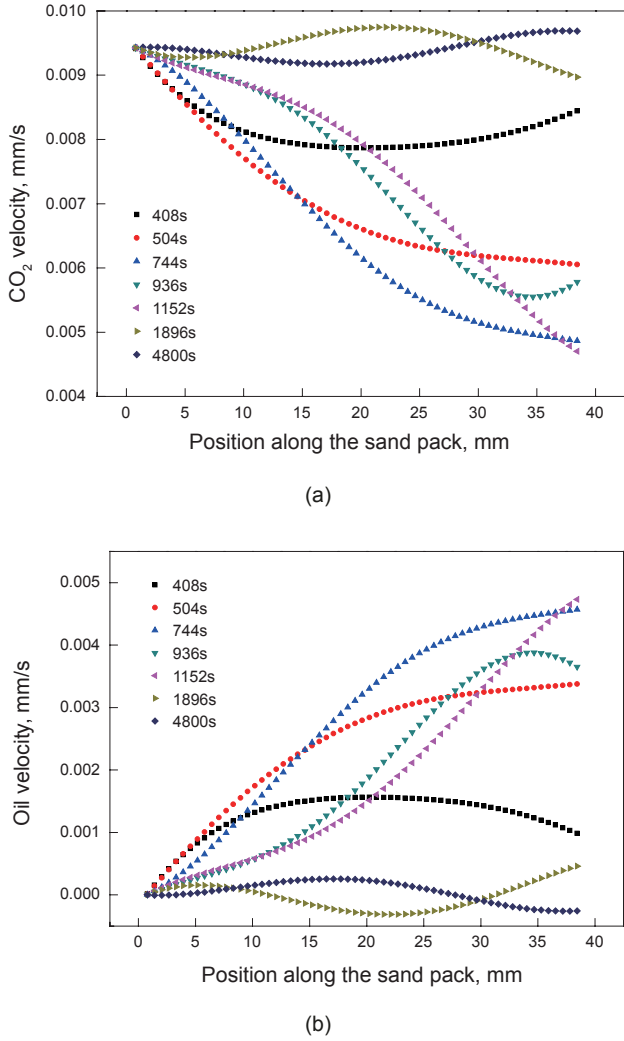
Fig. 10 Local phase velocities of (a) CO_2 and (b) oil

The capillary pressure $P_{co}(S_o)$ is defined in the standard convention by:

$$p_{co}(S_o) = p_g(S_o) - p_o(S_o) \qquad (9)$$

From Eqs. (8) and (9), the local Darcy velocity of CO_2 can be expressed as follows:

$$U_g = U(t)\frac{\lambda_g}{\lambda_g + \lambda_o}\left(1 + \frac{kg(\rho_o - \rho_g)}{U(t)}\lambda_o\right)$$
$$-k\frac{\lambda_g\lambda_o}{\lambda_g + \lambda_o}\frac{\mathrm{d}p_{co}}{\mathrm{d}S_o}\frac{\partial S_o}{\partial z} \qquad (10)$$

where U is the total flow rate.

The viscous-dominant fractional flow function, gravity countercurrent flow function, and the capillary dispersion rate can be defined as follows, respectively:

$$f_g(S_o) = \frac{\lambda_g}{\lambda_g + \lambda_o} \qquad (11)$$

$$G_g(S_o) = g(\rho_o - \rho_g)\frac{\lambda_g\lambda_o}{\lambda_g + \lambda_o} \qquad (12)$$

$$d_{cpo}(S_w) = -\frac{\lambda_g\lambda_o}{\lambda_g + \lambda_o}\frac{\mathrm{d}p_{co}}{\mathrm{d}S_o} \qquad (13)$$

Then Eq. (10) can be expressed as follows:

$$U_g = U(t)f_g(S_o) + kG_g(S_o) + kd_{cpo}(S_o)\frac{\partial S_o}{\partial z} \qquad (14)$$

And Eq. (14) can also be written as follows:

$$U_g = U(t)f_g^{(g)}(S_o, U) + kd_{cpo}(S_o)\frac{\partial S_o}{\partial z} \qquad (15)$$

with

$$f_g^{(g)}(S_o, U) = f_g(S_o) + \frac{k}{U}G_g(S_o) \qquad (16)$$

For any saturation S_o^*, the corresponding position in the sand pack can be expressed as a function of time:

$$S_o(z^*(t), t) = S_o^* \qquad (17)$$

Using this function, Eq. (15) can be written as follows:

$$U_g(z^*, t) = U(t)f_g^{(g)}(S_o^*, U) + kd_{cpo}(S_o^*)\frac{\partial S_o}{\partial z}\bigg|_{z^*, t} \qquad (18)$$

Except in the special case of zero total Darcy velocity (considered below), Eq. (18) can be rearranged to give:

$$\frac{U_g(z^*, t)}{U(t)} = f_g^{(g)}(S_o^*, U) + d_{cpo}(S_o^*)\frac{k}{U(t)}\frac{\partial S_o}{\partial z}\bigg|_{z^*, t} \qquad (19)$$

where $\dfrac{U_g(z^*, t)}{U(t)}$ and $\dfrac{k}{U(t)}\dfrac{\partial S_o}{\partial z}\bigg|_{z^*, t}$ are calculated from the observed saturation data. Provided gravity forces are negligible, or for periods of time when the total flow rate is constant, this equation gives $\dfrac{U_g(z^*, t)}{U(t)}$ as a linear function of $\dfrac{k}{U(t)}\dfrac{\partial S_o}{\partial z}\bigg|_{z^*, t}$, where the intercept is given by $f_g^{(g)}(S_o^*, U)$ and the gradient by $d_{cpo}(S_o^*)$. Thus plotting the observed values of $\dfrac{U_g(z^*, t)}{U(t)}$ against $\dfrac{k}{U(t)}\dfrac{\partial S_o}{\partial z}\bigg|_{z^*, t}$, $f_g^{(g)}(S_o^*, U)$ and $d_{cpo}(S_o^*)$ are estimated from the intercept and gradient of linear approximation of these data. The calculated capillary dispersion rate $d_{cpo}(S_o^*)$ is shown in Fig. 11.

It is worth noting that this capillary dispersion rate, which is used for reservoir simulation, can be estimated from only in-situ phase distribution data and the injection flow rate without additional measurements such as pressure drop across the sand pack. In other words, without the measurement of capillary pressure function p_{cw}, the capillary dispersion rate function can be evaluated. The capillary dispersion rate is a maximum at an oil saturation of 0.9.
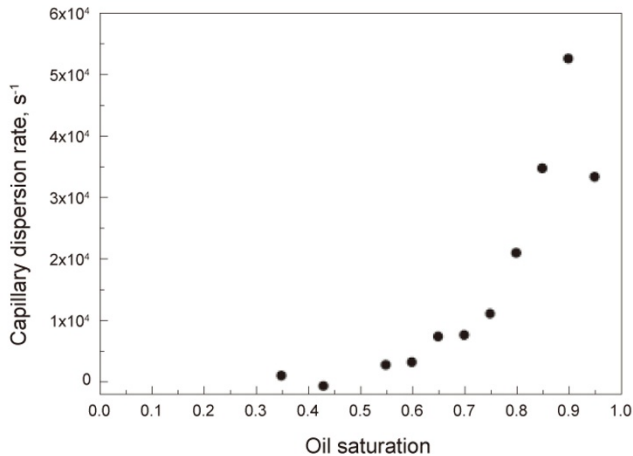
Fig. 11 Capillary dispersion rate at 8.1 MPa, 40 ºC

4 Conclusions

This article has provided experimental results on both gaseous CO_2 immiscible displacement and supercritical CO_2 miscible displacement of oil in high-permeable sand packs. The main conclusions are as follows:

1) A new high-pressure sand-pack cell was designed and constructed for the NMR imaging system with a RF probe of 40 mm inner diameter. The maximum working pressure and temperature of the sand-pack cell are 15 MPa and 80 ºC, respectively. By the high-pressure cell the process of CO_2 injected into the sand pack at high pressure and temperature can be visualized using NMR imaging.

2) The fundamental characteristics of the flooding process such as onset of CO_2 channeling or fingering, the piston-like front of CO_2, and the distribution of oil in porous media can be accurately detected.

3) It was found that for gaseous CO_2 immiscible displacement, CO_2 channeling or fingering occurred due to the difference in the viscosity and density of fluids, so the sweep efficiency was low and the final residual oil saturation was 53.1%. For supercritical CO_2 miscible displacement, piston-like displacement occurred, CO_2 channeling or fingering was restrained effectively, and the velocity of CO_2 front was uniform. The sweep efficiency was high and the final residual oil saturation was 33.9%. So supercritical CO_2 miscible displacement could enhance oil recovery more efficiency than gaseous CO_2 immiscible displacement.

4) The oil saturation distributions were monitored in-situ as function of volume of CO_2 injected, through analyzing the oil saturation profile the velocity of CO_2 front could be evaluated. A special core analysis method has been applied to in-situ oil saturation data to evaluate directly the local Darcy phase velocities and capillary dispersion rate.

Acknowledgements

References

Asghari K and Torabi F. Effect of miscible and immiscible CO_2 flooding on gravity drainage: Experimental and simulation results. Paper SPE 110587 presented at SPE/DOE Symposium on Improved Oil Recovery held in Tulsa, Oklahoma, USA, April 20-23, 2008

Aspenes E, Ersland G, Graue A, et al. Wetting phase bridges establish capillary continuity across open fractures and increase oil recovery in mixed-wet fractured chalk. Transport in Porous Media. 2008. 74(1): 35-47

Ayirala S C, Xu W and Rao D N. Interfacial behaviour of complex hydrocarbon fluids at elevated pressures and temperatures. The Canadian Journal of Chemical Engineering. 2006. 84(1): 22-32

Baldwin B A, Stevens J, Howard J J, et al. Using magnetic resonance imaging to monitor CH_4 hydrate formation and spontaneous conversion of CH_4 hydrate to CO_2 hydrate in porous media. Magnetic Resonance Imaging. 2009. 27(5): 720-726

Blackband S, Mansfield P, Barnes J R, et al. Discrimination of crude oil and water in sand and in bore cores with NMR imaging. SPE Formation Evaluation. 1986. 1(1): 31-34 (Paper SPE 13401)

Brautaset A, Ersland G, Graue A, et al. Using MRI to study in situ oil recovery during CO_2 injection in carbonates. Paper SCA 2008-41 presented at the International Symposium of the Society of Core Analysts held in Abu Dhabi, UAE, October 29-November 2, 2008a

Brautaset A, Ersland G and Graue A. In situ phase pressures and fluid saturation dynamics measured in waterfloods at various wettability conditions. Paper SPE 113510 presented at SPE/DOE Symposium on Improved Oil Recovery held in Tulsa, Oklahoma, USA, April 20-23, 2008b

Brunner R E and Mardock E S. A neutron method for measuring saturations in laboratory flow experiments. AIME Transactions. 1946. 165: 133-143

Callaghan P T. Principles of Nuclear Magnetic Resonance Microscopy. New York: Oxford University Press. 1994

Carr H Y and Purcell E M. Effects of diffusion on free precession in nuclear magnetic resonance experiments. Physical Review. 1954. 94(3): 630-638

Carretero-Carralero M D, Farajzadeh R, Du D X, et al. Modeling and CT-scan study of foams for acid diversion. Paper SPE 107795 presented at SPE European Formation Damage Conference held in Scheveningen, Netherlands, May 30-June 1, 2007

Chen Q, Rack F R. Balcom B J. Quantitative magnetic resonance imaging methods for core analysis. Geological Society, London, Special Publications. 2006. 267: 193-207

Chen S, Kim K H, Qin F, et al. Quantitative NMR imaging of multiphase flow in porous media. Magnetic Resonance Imaging. 1992. 10(5): 815-826

Chen S, Qin F, Kim K H, et al. NMR imaging of multiphase flow in porous media. AIChE Journal. 1993. 39(6): 925-934

Du D X, Beni A N, Farajzadeh R, et al. Effect of water solubility on carbon dioxide foam flow in porous media: An X-ray computed tomography study. Industrial & Engineering Chemistry Research. 2008. 47(16): 6298-6306

Du D X, Zitha P L J and Uijttenhout M G H. Carbon dioxide foam rheology in porous media: A CT scan study. SPE Journal. 2007. 12(2): 245-252 (Paper SPE 97552)

Ersland G, Husebø J, Graue A, et al. Measuring gas hydrate formation and exchange with CO_2 in Bentheim sandstone using MRI tomography. Chemical Engineering Journal. 2010. 158(1): 25-31

Fernø M A, Ersland G, Haugen Å, et al. Impacts from fractures on oil recovery mechanisms in carbonate rocks at oil-wet and water-wet

conditions—Visualizing fluid flow across fractures with MRI. Paper SPE 108699 presented at SPE International Oil Conference and Exhibition held in Veracruz, Mexico, June 27-30, 2007

Goodfield G, Goodyear S G and Townsley P H. New coreflood interpretation method for relative permeabilities based on direct processing of in-situ saturation data. Paper SPE 71490 presented at SPE Annual Technical Conference and Exhibition held in New Orleans, Louisiana, September 30-October 3, 2001

Hazlett R D, Gleeson J W, Laali H, et al. NMR imaging application to carbon dioxide miscible flooding in west Texas carbonates. Paper SCA 9311 presented at the Annual technical conference proceedings: Society of Professional Well Log Analysts, Society of Core Analysts Chapter-at-Large, 1993

Hunt P K and Bajsarowicz C. Computed tomography as a core analysis tool: Applications, instrument evaluation, and image improvement techniques. Journal of Petroleum Technology. 1988. 40(9): 1203-1210 (Paper SPE 16952)

Kantzas A. Recent advances in the characterization of porous media using computer assisted tomography of X-rays. Canada Well Logging Society Journal. 1995. 20: 99-102

Laird A D K and Putuan J A. Fluid saturation in porous media by X-ray technique. Petroleum Transactions, AIME. 1951. 192: 275-284 (Paper SPE 951275)

Meiboom S and Gill D. Modified spin-echo method for measuring nuclear relaxation times. Review of Scientific Instruments. 1958. 29(8): 688-691

Morgan F, McDowell J M and Doty E C. Improvements in the X-ray saturation technique of studying fluid flow. Petroleum Transactions, AIME. 1950. 189: 183-194 (Paper SPE 950183)

Perkins T K and Johnston O C. A study of immiscible fingering in linear models. SPE Journal. 1969. 9(1): 39-46 (Paper SPE 2230)

Romero-Zeron L, Ongsurakul S, Li L, et al. Visualization of waterflooding through unconsolidated porous media using magnetic resonance imaging. Petroleum Science and Technology. 2009. 27(17): 1532-2459

Romero-Zeron L, Ongsurakul S, Li L, et al. Visualization of the effect of porous media wettability on polymer flooding performance through unconsolidated porous media using magnetic resonance imaging. Petroleum Science and Technology. 2010. 28(1): 52-67

Suekane T, Furukawa N, Tsushima S, et al. Application of MRI in the measurement of two-phase flow of supercritical CO_2 and water in porous rocks. Journal of Porous Media. 2009. 12(2): 143-151

Suekane T, Ishii T, Tsushima S, et al. Migration of CO_2 in porous media filled with water. Journal of Thermal Science and Technology. 2006. 1(1): 1-11

Suekane T, Sokawa S, Iwatani S, et al. Behavior of supercritical CO_2 injected into porous media containing water. Energy. 2005. 30(11): 2370-2382

Vinegar H J. X-ray CT and NMR imaging of rocks. Journal of Petroleum Technology. 1986. 38(3): 257-259 (Paper SPE 15277)

Wellington S L and Vinegar H J. CT studies of surfactant induced CO_2 mobility control. Paper SPE 14393 presented at SPE Annual Technical Conference and Exhibition held in Las Vegas, Nevada, September 22-26, 1985

Wellington S L and Vinegar H J. X-ray computerized tomography. Journal of Petroleum Technology. 1987. 39(8): 885-898 (Paper SPE 16983)

Wooding R A. Growth of fingers at an unstable diffusing interface in a porous medium or Hele-Shaw cell. Journal of Fluid Mechanics. 1969. 39: 477-495

(Edited by Sun Yanhua)